

Measurement of Colloidal Forces with TIRM

Dennis C. Prieve
Department of Chemical Engineering
Carnegie Mellon University
Pittsburgh, PA 15213
email: dcprieve@cmu.edu

Keywords: colloidal forces, surface forces, double-layer repulsion, van der Waals attraction, evanescent wave

Abstract

During the last ten years, we have developed a new experimental technique called Total Internal Reflection Microscopy. Using TIRM we can monitor the separation distance between a single microscopic sphere immersed in an aqueous solution and a transparent plate. Because the distance is calculated from the intensity of light scattered by the sphere (3 to 30 microns in diameter) when illuminated by an evanescent wave, this technique provides a sensitive, nonintrusive, and instantaneous measure of the distance between the sphere and the plate. Changes in distance as small as 1 nm can be detected.

From the equilibrium distribution of separation distances sampled by Brownian motion, we determine the potential energy profile in the vicinity of the minimum formed by gravitational attraction and double-layer repulsion or steric repulsion caused by adsorbed soluble polymer. Forces as small as 0.01 piconewtons can be detected. We have also measured van der Waals attraction, the radiation pressure exerted by a focussed laser beam, receptor-mediated interaction between antigen and antibodies, and steric repulsion due to adsorbed polymer layers.

From the autocorrelation of the temporal fluctuations in scattering intensity, we have inferred the value of the normal component of the diffusion coefficient, which is about two orders of magnitude smaller than the bulk value owing to the close proximity of the sphere to the wall. This provides the first experimental test of Einstein's equation (relating mobility and diffusion coefficient) in a colloidal force field.

1. Introduction

During the last ten years, we have been developing a new experimental technique for measuring the colloidal interaction between a single microscopic particle and a flat plate in an aqueous environment. We are able to measure the force without touching the particle, and while the particle remains free to undergo Brownian motion. We call our technique Total Internal Reflection Microscopy or “TIRM” [1]. More generally, TIRM is a technique for monitoring the instantaneous separation distance between the sphere and the plate. From the equilibrium distribution of separations sampled by Brownian motion, we can determine the potential energy of interaction; from the time-dependence of the separation distance, we can either determine the hydrodynamic mobility or diffusion coefficient of the sphere. In this overview, we will describe this new technique (Sect. 2), review some of the results we have observed (Sects. 3 and 4), and compare TIRM with more familiar techniques like the Surface Forces Apparatus or Atomic Force Microscopy (Sect. 5).

2. The Technique

So far we have mainly studied the interaction of polystyrene (PS) latex or glass spheres and a glass plate, sometimes with coatings on either or both surfaces, when the two bodies are separated by an aqueous solution. Both glass and PS are more dense than water, so a single sphere of several microns size, constructed of either material, will settle by gravity to the bottom of the container, which is usually a glass microscope slide. We arrange the experimental conditions so the sphere is prevented from coming into intimate contact with the slide by some sort of colloidal repulsion. For example, if both surfaces are similarly charged, the sphere experiences double-layer repulsion, which increases in strength as it approaches the slide. If the surfaces have enough charge and the ionic strength of the solution is not too high, there will be one particular separation distance at which the double-layer repulsion and gravitational attraction are exactly balanced. Although this elevation corresponds to mechanical equilibrium, the sphere does not remain stationary at this particular location after settling.

Instead the sphere will sample elevations above and below this equilibrium value by Brownian motion (see Fig. 1). The probability of finding it at any particular location depends on the potential energy (PE) at that location: locations having high PE are sampled less frequently than locations having lower PE. The quantitative relation between the PE and the number of times different elevations are sampled is given by Boltzmann's equation:

$$p(h) = A \exp \left[-\frac{\phi(h)}{kT} \right] \quad (1)$$

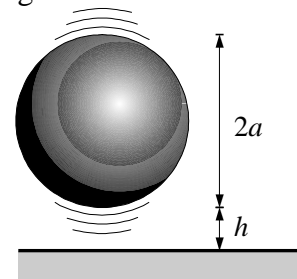


Fig. 1

TIRM measures the interaction between a single microscopic sphere and a flat plate by monitoring the Brownian fluctuations in separation distance, h .

where $p(h)dh$ is the probability of finding the sphere between h and $h+dh$, $\phi(h)$ is the PE of the sphere at elevation h , kT is the thermal energy and A is a normalization constant whose value is chosen such that $\int p(h)dh = 1$.

If only gravity and double-layer repulsion act, the PE profile $\phi(h)$ should look something like shown in the top of Fig. 2. When the sphere is far from the plate, it is outside the range of interactions with the plate, leaving gravity as the dominant force: then PE increases linearly with separation distance. When the sphere ventures close to the plate, it experiences double-layer repulsion which causes the PE to increase as the separation decreases. Substituting the $\phi(h)$ shown in the top half of Fig. 2 into (1) yields the probability density profile $p(h)$ shown in the bottom half of Fig. 2. The Boltzmann distribution means that, the lower the particle's PE at a given location, the more likely it is to find the particle at that location. Thus the most probable location corresponds to the bottom of the PE well, where gravity and double-layer repulsion are equal.

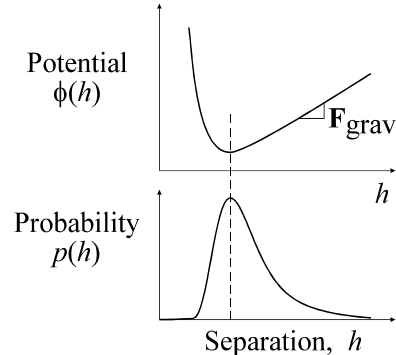


Fig. 2.
A typical PE profile (top) with the associated probability density predicted by Boltzmann's equation (1) (bottom).

2.1 Measuring the Potential

More generally, TIRM is a technique for monitoring the instantaneous separation distance, h . After taking one measurement, we wait for the distance to change by Brownian motion before taking a second measurement. We then repeat this process a statistically large number of times: typically we take 50,000 measurements of the separation at 10 ms intervals. We then form a histogram of these 50,000 measurements. If the particle has had time to sample all elevations a statistically large number of times, this histogram converges to the probability density function $p(h)$ appearing in Boltzmann's equation.

In essence, TIRM is then capable of directly measuring this probability density function. Knowing $p(h)$, we can turn Boltzmann's equation (1) "inside-out" to deduce the PE profile $\phi(h)$: to eliminate A , we divide (1) by (1) evaluated at some reference position denoted h_m before solving for the PE. This leaves

$$\frac{\phi(h) - \phi(h_m)}{kT} = \ln \frac{p(h_m)}{p(h)} \quad (2)$$

Usually h_m is chosen as the elevation corresponding to the minimum in $\phi(h)$. Since Boltzmann's equation defines the mean potential in statistical mechanics, we claim that TIRM directly measures the PE profile. The idea of using Boltzmann's equation to measure the PE profile for colloidal forces was suggested earlier by Alexander and Prieve [2, 3], although they used a hydrodynamic technique to measure the instantaneous separation distance rather than TIRM.

2.2 Measuring the Separation Distance

To determine the instantaneous separation distance, we measure the intensity of light scattered by the sphere when it's illuminated by an evanescent wave, produced by reflecting a laser beam off the glass-water interface at a sufficiently glancing angle so that total reflection occurs.

Total internal reflection can only occur when the incident ray passes through a medium having a higher refractive index than that of the medium on the other side of the interface. In our case, the incident medium is glass ($n_1 = 1.52$), which has a higher refractive index than water ($n_2 = 1.33$). When $n_1 > n_2$ Snell's law

$$n_1 \sin \theta_i = n_2 \sin \theta_r$$

predicts that the refracted ray is bent away from the normal as shown in Fig. 3; i.e. $\theta_r > \theta_i$. This is an "internal reflection." As the angle of incidence is increased, the refracted ray eventually becomes parallel to the interface (i.e. $\sin \theta_r = 1$) at one particular angle of incidence, called the "critical angle":

$$\theta_{i,crit} = \sin^{-1} \frac{n_2}{n_1}$$

which equals about 61° at our glass/water interface. If $\theta_i > \theta_{i,crit}$ the refracted ray disappears and the incident light undergoes "total internal reflection." Although no net energy is transferred to the water under conditions of total internal reflection, an optical disturbance occurs in the water which takes the form of an "evanescent wave" [4]. Instead of varying sinusoidally with distance in all directions (like the incident plane wave), the electric field associated with an evanescent wave decays exponentially with distance from the interface. Thus only water very near the interface is illuminated by the evanescent wave.

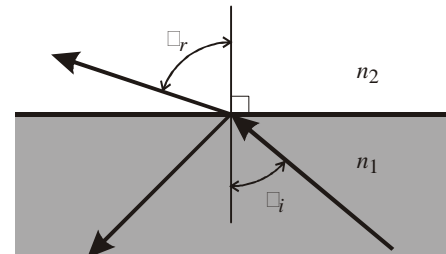


Fig. 3
Internal reflection of a ray.

When a sphere with a refractive index different from that of the water settles near an interface at which total internal reflection occurs, some of the evanescent wave is scattered as shown in Fig. 4; this situation is called “frustrated” total internal reflection [4]. Because of the nonuniform illumination of the water by the evanescent wave, the amount of light scattered by the sphere is exquisitely sensitive to its proximity to the interface.

Chew *et al.* [5] solved the Mie scattering problem for a one-micron sphere illuminated by an evanescent wave. Their solution reveals that the intensity of scattering is a complicated function of direction, involving multiple peaks and valleys. However, TIRM integrates the scattered intensity over a cone of solid angle corresponding to the numerical aperture of the microscope objective lens; moreover, Chew *et al.* [5] found that the intensity of scattering in any direction decays exponentially with elevation of the sphere above the plate. Thus the integrated scattering intensity sensed by the PMT should also decay exponentially with elevation.

However, the analysis of Chew *et al.* [5] ignores the plate except for generating the evanescent wave. When the sphere is replaced by a half-space, the evanescent energy flux “tunnelling” through a thin film, separating it from another half-space, decays exponentially with film thickness only for thick films [6]. For thin films, the energy flux is less sensitive to film thickness owing to multiple reflections of rays between the two half-spaces. Multiple reflections between the sphere and the plate are not considered by Chew *et al.*

Prieve & Walz [7] used ray-optics to calculate the distribution of scattering of the evanescent wave from spheres which are large compared to the wavelength. In addition to multiple reflections of rays inside the sphere, they also considered multiple reflections between the sphere and the plate. They found that, for spheres of 30 μm or smaller, rays scattered toward the plate do not again encounter the sphere. Like Chew *et al.*, they found that the intensity of scattering in any direction decays exponentially with elevation of the sphere above the plate.

Prieve & Walz [7] also devised a method for placing the sphere a known and adjustable distance from the wall, and measured the scattering intensity as a function of distance, using the same apparatus described above. A MgF_2 film was sputtered onto a glass slide which serves as a spacer to separate the PS sphere from the glass plate by a distance equal to the known film thickness. The fluid (a mixture of propanol and ethanol) was chosen to have the same refractive index as the film; then the interface between the outer film and the fluid disappears, leaving the same scattering geometry as in our usual TIRM experiments.

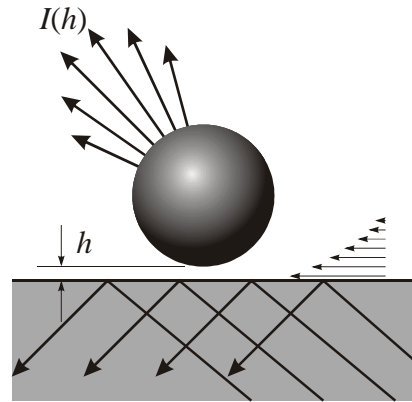


Fig. 4
When illuminated by an evanescent wave (horizontal arrows), the sphere scatters light which is exponentially sensitive to its elevation h .

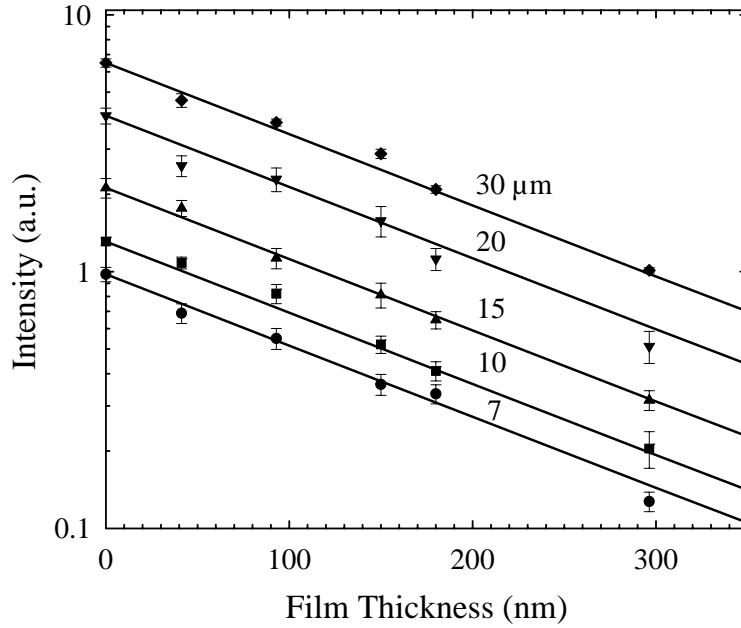


Fig. 5

Scattering of PS spheres resting on a MgF_2 film coating a glass microscope slide. The fluid is index matched to the film. Replotted from [7].

Fig. 5 summarizes the measured scattering intensity as a function of film thickness for spheres of different diameter. The results for different size spheres have been offset for ease of viewing (the effect of sphere size on scattering is discussed below in Section 6). Each point is the average of about 20 measurements for different spheres of the same diameter, which scatter quite differently (possibly due to different density inhomogeneities within each particle). The lines all have a slope β calculated from

$$\beta = \frac{4\pi}{\lambda} \sqrt{(n_1 \sin \theta_i)^2 - n_2^2}$$

where β^{-1} is the penetration depth of the evanescent wave intensity. The points representing average scattering intensities virtually all fall within experimental uncertainty of these lines. This confirms the ray-optics predictions that the scattering intensity I decays with the same dependence on distance from the wall as the intensity of the evanescent wave itself:

$$I(h) = I_0 e^{-\beta h} \quad (3)$$

Typically β^{-1} is about 100 nm in our experiments in aqueous solutions. Because of this exponential sensitivity, a very small change in h produces a measurable change in intensity. For example, we estimate that the photomultiplier tube we use to quantify the light intensity can realistically detect a 1% change in intensity. According to (3) with $\beta^{-1} = 100$ nm, a 1% change

in I corresponds to a 1 nm change in h . Thus we can detect changes in h of the order of 1 nm, which represents the current spatial resolution of the technique.

To obtain absolute separation distance, we need a value for I_0 in (3). The data in Fig. 5 show that (3) holds for all separations including contact ($h = 0$) despite the possibility of multiple reflections between the sphere and the plate (provided the sphere is not too large). Thus I_0 can be directly measured by forcing the sphere into intimate contact with the wall. For spheres levitated by double-layer repulsion, this can be accomplished by increasing the ionic strength of the solution to about 10 mM. Then double-layer repulsion is sufficiently weakened that van der Waals attraction causes the sphere to jump into intimate contact, allowing I_0 to be measured.

2.3 Apparatus

Fig. 6 shows a schematic of the TIRM flowcell. A syringe is used to inject salt solution containing latex particles (typically 3 to 30 μm in diameter) between two microscope slides optically coupled to a dove-tail prism. The two slides are held about 1 mm apart using an o-ring as a spacer. After 10-20 minutes, the particles have settled near the lower slide. The flowcell is mounted on a specially designed micrometer stage, which allows 3D motion relative to the objective lens of the microscope. This stage is adjusted until a single levitated particle is in the field of view of the objective lens and the particle appears focussed.

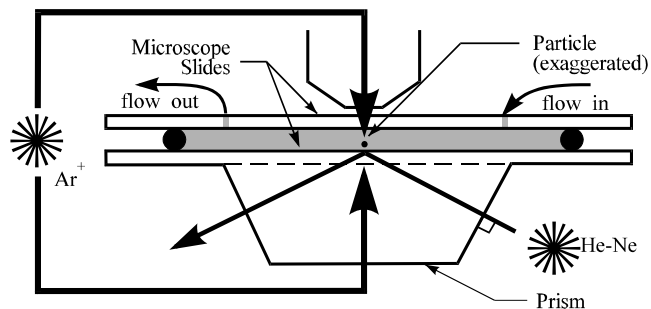


Fig. 6.

A schematic of the TIRM flowcell. The He-Ne laser generates the evanescent wave used to monitor the elevation of the particle, while the Ar^+ laser is used to create a 2D optical trap in the horizontal plane and to exert an upward or downward force on the particle.

Depending primarily on the pre-treatment of the glass slide, some or all of the particles might stick to the glass. A stuck particle will not move when additional fluid is injected into the flowcell. Sticking is usually the result of insufficient charge at low ionic strengths (in the case of double-layer repulsion; or insufficient adsorbed polymer, in the case of steric repulsion) on the surface of either the sphere or the plate. To increase the negative charge on the glass plate, we soak our slides in a basic solution before rinsing and mounting in the TIRM apparatus. Similarly, dilution of surfactant-stabilized particles might cause desorption of the ionic surfactant, loss of charge, and sticking of the particles. This can be avoided by using sulfonated or carboxylated latexes having covalently attached charges; or the particles might be dispersed in a solution of anionic surfactant like SDS. Of course, the total ionic strength must also be kept below about 5 mM to keep most of the particles levitated.

A 30 mW helium-neon laser beam is made incident to the water-glass interface at an angle greater than the critical angle so that total internal reflection results. A reproducible angle of incidence is accurately set by adjusting a mirror mounted on a rotating micrometer stage until the beam reflected off the incident face of the prism practically coincides with the incident beam;

this gives normal incidence for the external reflection at the air-glass interface and an angle of incidence for the internal reflection at the glass-water interface equal to the angle between the two faces of the prism (68°). The rotating stage containing the mirror is in turn mounted on a 2D

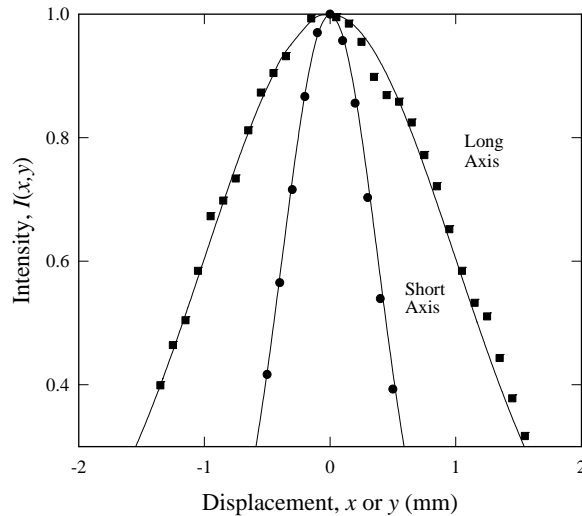


Fig. 7
Intensity of a stuck particle illuminated by the evanescent wave as the particle is displaced from the center of the beam by moving the stage right and left (long axis) or front and back (short axis). Replotted from Fig. 2-8 in [8].

translation stage which is now adjusted until the light scattered from the particle is maximized; this corresponds to centering the internal reflection under the particle.

If desired, the angle of incidence for the internal reflection can be determined by measuring the time-averaged scattering from a stuck particle as the 2D stage bearing the mirror is slowly translated left and right (the x position), then front and back (the y position). Some typical results are shown in Fig. 7 [8]. For a Gaussian beam, the intensity should be a Gaussian function of either x or y , although the half-widths of the two Gaussians are not equal. For non-normal incidence at the glass-water interface, the circular symmetry of the incident Gaussian beam is distorted into an ellipse. The ratio of the major axis to the minor axis of the ellipse (which equals the ratio of the half-widths of the two Gaussians in Fig. 7) is related to the angle of incidence. Thus Walz & Prieve [9] determined the angle of incidence for the prism of Fig. 6 to be $67.8 \pm 0.3^\circ$.

At this point, when properly levitated, the particle appears in the microscope as a bright spot on a dark field, its intensity continually flickering brighter or dimmer as Brownian motion moves the particle closer or further from the plate. The 300 mW argon-ion laser (heavy arrows in Fig. 6) generates a 2D optical trap which keeps the sphere centered in the observation area. The trap is sufficiently strong to hold the particle while the surrounding fluid is gently replaced. This

beam can also be used to exert an upward or downward force on the particle. Measurements of the optical force is discussed below in Fig. 14.

Details of the optical train for the upward beam can be found in [9] or [10], while details for the downward beam can be found in [8]. Basically, the more familiar 3D optical traps use a very short focal length (1-2 mm) objective lens to focus the laser beam; this produces a beam with high divergence near the waist. Instead, we focus the laser beam using a long focal length (10 cm) lens before it enters the objective. This produces a beam with low divergence which exerts an axial force on the particle which is relatively insensitive to axial position. The beam leaving the laser is split according to its polarization to form both the upward and downward beams. The distribution of power between the upward and downward beams is adjusted by rotating a quartz half-wave retardation plate which controls the polarization.

Most of the experimental results reviewed in this manuscript were obtained using the P-01 photometry system which is an accessory to our Zeiss Universal microscope. This photometry system generates an electrical analog output which is sampled by a personal computer after passing through an A/D converter. Even when exposed to a constant light source, the analog output displays fluctuations of 2-10% of the mean intensity, depending on the gain and on the percent of full scale [11]. Because all fluctuations are attributed to Brownian motion, any instrument noise causes some distortion in the deduced PE profile. Simulations like those in Prieve & Frej [12] can be used to estimate the distortion. Such distortion becomes significant when measuring interactions having an exponential decay length (e.g. Debye length) less than 10 nm. Recently we have switched from analog to digital data acquisition (single photon counting) as a means of alleviating instrument noise.

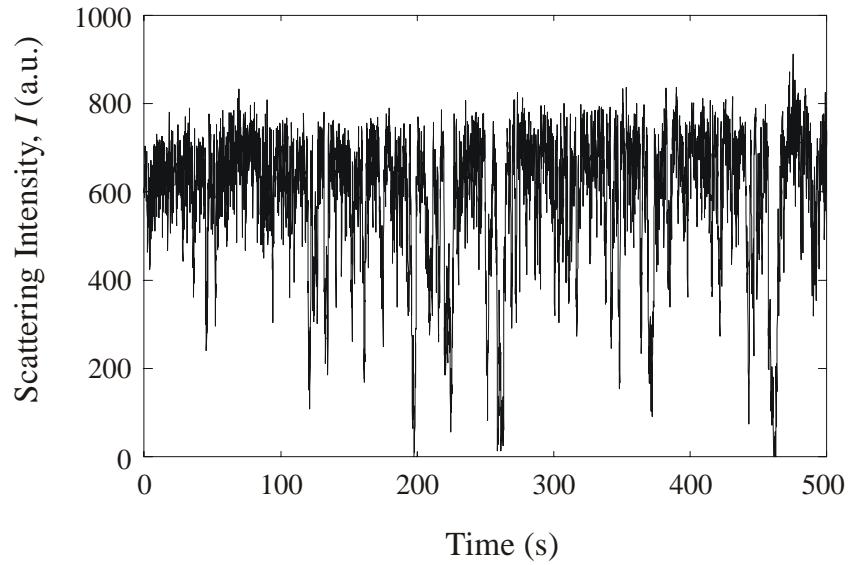


Fig. 8
Fluctuations in scattering observed for a 9.87 μm PS latex sphere in 0.5 mM NaCl solution (replotted from Fig. 3-1 in [10]). The occasional drop to near zero intensity corresponds to an excursion by to the sphere to very large elevations above the glass slide.

2.4 Analysis of Data

Fig. 8 shows some typical raw data: 50,000 readings of scattering intensity recorded at 10 ms intervals. If the Brownian sphere has had plenty of time to sample elevations in some reasonable interval of elevations many times within the set of observations made with TIRM, then the *shape* of a histogram of elevations $n(h)$ is the same as the *shape* of the probability density function $p(h)$ over this interval of elevations. In other words, $n(h)$ is directly proportional to $p(h)$ and the ratio of probabilities in (2) can be replaced by the ratio of the number of observations in the corresponding bins of the histogram. This means that the PE profile can be deduced from the histogram using

$$\frac{\phi(h) - \phi(h_m)}{kT} = \ln \frac{n(h_m)}{n(h)}$$

This requires that all the bins of the histogram $n(h)$ must have equal width Δh and that Δh must be small enough that $\Delta h \rightarrow dh$. If each measurement of intensity I is separately converted into a corresponding elevation h , then construction of such a histogram is straightforward.

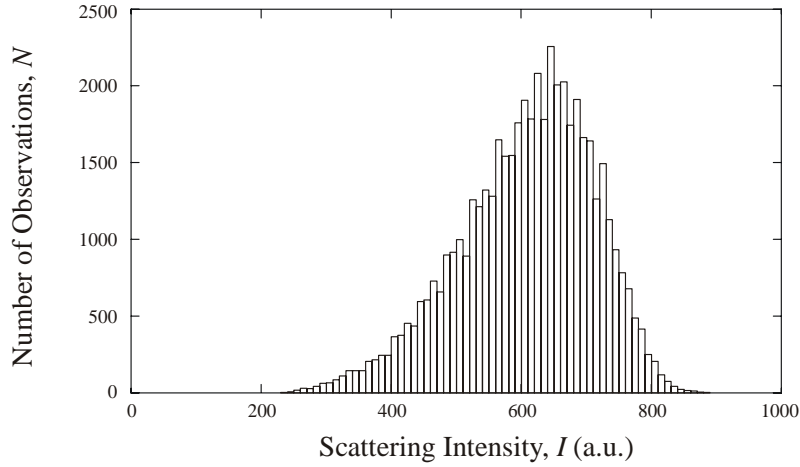


Fig. 9
The histogram of scattering intensities condensed from the 50,000 readings of Fig. 8
(replotted from Fig. 3-2 in [10]).

As an alternative which avoids this conversion, we work directly with the histogram of the intensities $N(I)$, where $N(I)$ is the number of observations of intensity in the range from I to $I+\Delta I$: see Fig. 9. The probability density for intensity $P(I)$ can be related to the probability density for elevation $p(h)$ by observing that the number of observations of intensity in the range from I to $I+dI$ is equal to the number of observations of elevation in the corresponding range from h to $h+dh$ [1]:

$$P(I)dI = p(h)dh$$

or

$$p(h) = P(I) \frac{dI}{dh} = -\beta P(I) I(h) \quad (4)$$

where the second equality is obtained with the help of (3). After substituting (4), (2) becomes

$$\frac{\phi(h) - \phi(h_m)}{kT} = \ln \frac{N(I_m) I_m}{N(I) I} \quad (5)$$

where $I_m = I(h_m)$. If the histogram of intensities has bins of equal width ΔI and if ΔI is small then $P(I)$ and $P(I_m)$ can be replaced by $N(I)$ and $N(I_m)$, which has already been assumed in (5). The extra factor I_m/I appearing in the argument of the logarithm essentially accounts for having equal bin widths in intensity I , instead of equal bin widths in h .

3. Results: PE Profiles

3.1 Gravity and Double-Layer Repulsion

Expected shape. When the separation distance is several Debye lengths, we expect van der Waals attraction to be severely retarded and screened and double-layer repulsion to be well modelled using linear superposition and Derjaguin's approximations. Then, for a 1:1 electrolyte, the total PE profile is expected to obey

$$\phi(h) = B \exp(-\kappa h) + Gh \quad (6)$$

where

$$B = 16\epsilon a \left(\frac{kT}{e}\right)^2 \tanh\left(\frac{e\psi_1}{4kT}\right) \tanh\left(\frac{e\psi_2}{4kT}\right) \quad (7)$$

ϵ is the dielectric permittivity of water, a is the radius of the sphere, e is the elemental charge, ψ_1 and ψ_2 are the Stern potentials of the sphere and the plate,

$$\kappa = \sqrt{\frac{8\pi C e^2}{\epsilon kT}} \quad (8)$$

is the Debye parameter, C is the total ionic strength, and

$$G = \frac{4}{3} \pi a^3 (\rho_s - \rho_f) g \quad (9)$$

is the net weight of the sphere. (6) has a single minimum at

$$\kappa h_m = \ln \frac{\kappa B}{G} \quad (10)$$

The charge parameter B is difficult to determine independently. Fortunately, we can eliminate B between (6) and (10) to obtain the relative PE in terms of the relative separation distance $h-h_m$:

$$\frac{\phi(h) - \phi(h_m)}{kT} = \frac{G}{\kappa kT} \left\{ \exp[-\kappa(h - h_m)] - 1 \right\} + \frac{G}{kT} (h - h_m) \quad (11)$$

In other words, the *shape* of the PE profile is not affected by B . Increasing the charge on either the sphere or the plate will shift the minimum to larger separation distances h_m according to (10), but it does not affect the shape.

Hydrodynamic Repulsion. Why does hydrodynamic repulsion — which increases as the particle approaches the plate and is known to decrease the rates of flocculation [13] — not appear as a contribution to the expected PE profile of either (6) or (11)? The simple answer is that its effect cancels out of the equilibrium distribution of elevations. Qualitatively, the hydrodynamic drag force acts in a direction opposite to the direction of motion of the particle.

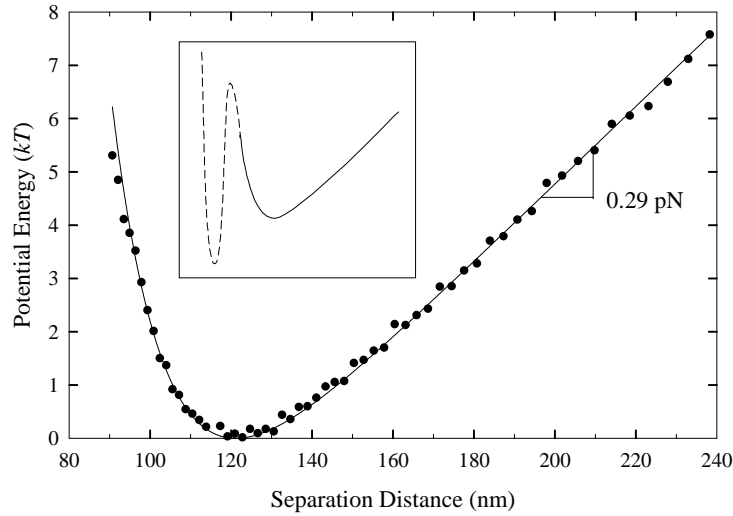


Fig. 10

The PE profile deduced from the histogram in Fig. 9 with the help of (5) (replotted from Fig. 3-3 in [10]). The solid curve is (11) with $G = 0.29$ pN, $\kappa^{-1} = 12.9$ nm and $h_m = 120$ nm. The insert shows the expected PE profile for smaller separations.

Half the time, the particle is moving toward the plate while the other half of the time it's moving away from the plate. The time-average hydrodynamic drag force vanishes at equilibrium. Quantitatively, Boltzmann's distribution can be derived by noting that the net flux of particles from diffusion and migration in the colloidal force field vanishes at equilibrium:

$$\text{flux} = -D(h) \frac{dp}{dh} - m(h) \frac{d\phi}{dh} p = 0 \quad (12)$$

Owing to hydrodynamic repulsion, both the diffusion coefficient D and mobility m vanish as the particle approaches the plate (as $h \rightarrow 0$), but the two coefficients are directly proportional according to Einstein's equation:

$$D(h) = m(h)kT \quad (13)$$

Dividing (12) by $D(h)$, substituting (13), then integrating yields Boltzmann's equation (6). Both position-dependent coefficients cancel, leaving the constant kT . Thus hydrodynamic drag does not affect the equilibrium distribution of elevations, nor does the position dependence of the drag force. Of course, this increase in hydrodynamic drag does reduce the flocculation rates, but flocculation is not an equilibrium process and the right-hand-side of (12) is not zero. Measurements of the drag force (or mobility) are discussed below in Fig. 19.

Fig. 10 shows some typical experimental results for the PE profile obtained with TIRM. This particular profile is near the secondary minimum formed by gravitational attraction and double-layer repulsion. At separations smaller than sampled in Fig. 10, we expect van der Waals

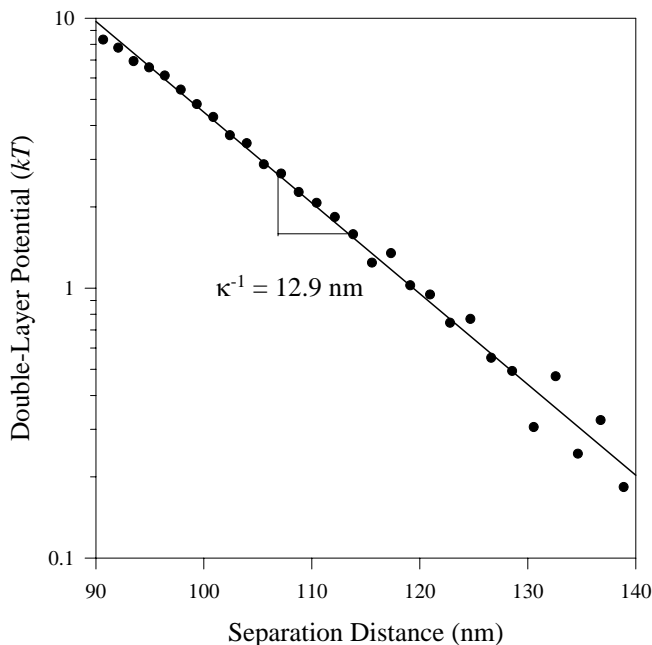


Fig. 11
Double-layer contribution to the PE profile obtained by subtracting gravity from Fig. 10.

attraction to become important, which would form a maximum and a deep primary PE well (see insert).

Notice that at large elevations, the profile in Fig. 10 becomes linear. This is because far from the surface the sphere is outside the range of surface forces and only gravity is important. The PE from gravity increases linearly with elevation. The slope should correspond to the known weight of the sphere. From a regression of the linear portion of the profile, we measure a net weight of 0.29 pN. We can also calculate the net weight from (9); using the known size and density (1.055 g/cm³) of the sphere, (9) yields 0.27 pN. The measured and calculated weights are within a few percent of each other. Similar agreement was obtained for PS spheres having a diameter between 7 and 15 μm [12, 14]; thus net weights as small as 0.09 pN were measured and found to be within $\pm 6\%$ of the calculated weights. This agreement is a strong confirmation of this technique for measuring forces.

Note that the magnitude of the forces measured with TIRM are approximately 100 times smaller than what can be achieved with either SFA or AFM. More will be said about this comparison in Section 5.1. But first, let's take a look at the colloidal forces acting on the sphere.

Subtracting out the contribution from gravity leaves the contribution from colloidal interactions: see Fig. 11. If this is primarily double-layer repulsion, we would expect an exponentially decaying potential [see the first term in (6)], which would be linear when plotted on this semi-log plot. Indeed, the points in Fig. 11 do seem to fall along a straight line. From the slope of the regression line, we can deduce an apparent Debye length of about 12.9 nm,

which is reasonably close to $\kappa^{-1} = 13.6$ nm calculated from (8) using the known ionic strength of the solution.

The intercept of Fig. 11 yields $B = 1.03 \times 10^4 kT$ which could be compared with the predictions of (7) if values of ψ_1 and ψ_2 were available. Unfortunately, we are not yet equipped to measure both potentials in independent experiments. Assuming the two Stern potentials are equal, we deduce ± 31 mV as the average Stern potential. This is the order-of-magnitude expected for such potentials. In the future, if the Stern potential of one of the two surfaces were known, we might use the results of a regression like that in Fig. 11 to deduce the Stern potential of the other surface. If both interacting bodies are composed of the same material, the two Stern potentials might be equated and their common value can then be deduced from B .

Since few techniques exist which can measure the Stern potential (the potential drop across the diffuse cloud of the double layer), it is usually equated with zeta potential (the potential drop between the shear plane and the bulk). Larson *et al.* [15-17] recently compared Stern potentials measured with AFM between a silica, alumina or titania microsphere and a plate composed of the same oxide with zeta potentials measured for the same oxide. In nearly every case, the two potentials were equal.

Substituting $B = 1.03 \times 10^4 kT$ into (10), we predict $h_m = 120$ nm, which is almost exactly where the minimum in Fig. 10 occurs. Using TIRM for PS spheres between 7 and 15 μm in diameter, Bike *et al.* [18-20] observed close agreement between the exponential decay lengths regressed from plots like Fig. 11 and the Debye length, provided the ionic strength remains less than about 1 mM. The most probable separation distance turns out to be 7-10 Debye lengths, which is why the simple exponential decay fits so well. Above about 1 mM ionic strength, the sphere comes close enough to the plate to experience significant van der Waals attraction.

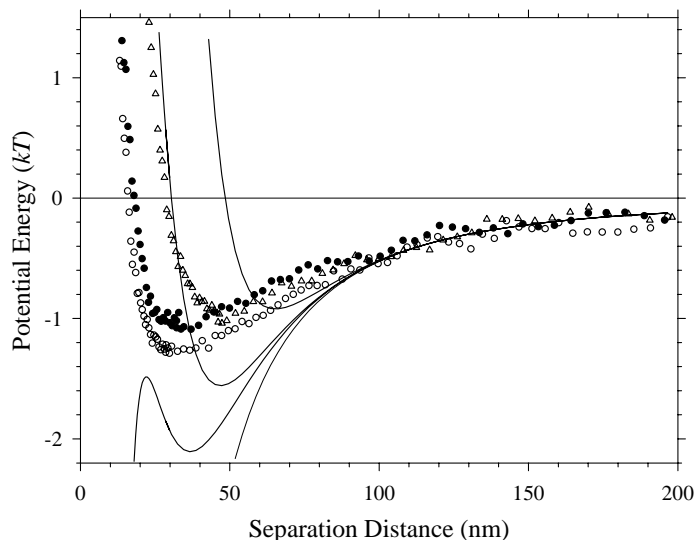


Fig. 12
Colloidal interactions between a 6.24 μm PS sphere interacting with a glass slide (coated with a 1 μm PS film) across a solution containing 1.1 mM SDS [21]. Curves are predictions which consider retarded van der Waals attraction (lowest curve) and double-layer repulsion.

3.2 van der Waals Attraction

Fig. 12 shows a PE profile measured with TIRM which shows a significant van der Waals attraction. The gravitational contribution to the PE has already been subtracted. Unlike the results of Fig. 11 in which the colloidal interaction decays monotonically to zero, the profile of Fig. 12 displays a significant minimum. Van der Waals attraction dominates in the portion of the profile having a positive slope whereas double-layer repulsion again dominates in the portion having negative slope. Van der Waals attraction is probably not important in Fig. 11 because a much higher charge on the glass (compared to that on the PS) pushed the particle out to larger separations where van der Waals attraction is negligible.

To predict van der Waals attraction using Lifshitz theory, we need the dielectric spectra of the materials. Since detailed spectra are available for PS and water [22], but not for glass, we coated the glass slide used in Fig. 12 with a film of PS. To obtain a significant charge on the PS film, we added an anionic surfactant (SDS) in the aqueous solution. Lifshitz theory was used to calculate the retarded van der Waals attraction between two PS half-spaces across an aqueous solution. Parsegian's correction [22] for Debye screening was applied to the zero-frequency term. Derjaguin's approximation was used to calculate the sphere-plate interaction from that for two half-spaces [23]. To this van der Waals energy is added a contribution from double-layer repulsion which takes the form of the first term in (6). Since the charge parameter B is unknown,

we tried three different reasonable values ($B = 135, 190$ and $500 kT$) to obtain the three curves of the total predicted PE shown in Fig. 12.

None of the curves is a reasonable fit of the experimental PE profile. Indeed no value for the single adjustable parameter (B) leads to reasonable agreement between theory and experiment. The measurements of van der Waals attraction appear weaker than those predicted by this theory. Previous measurements of van der Waals attraction with TIRM [10, 24] have also found weaker attraction than expected from Lifshitz theory. Roughness of either surface was suggested as the explanation, although these earlier experiments used glass or mica whose dielectric spectra must be estimated.

3.3 Optical Forces

The idea that light can exert a force is at least as old as the astronomer Kepler (1571-1630) who suggested that the tails of comets point away from the sun because the sun exerts a force on them. To understand the nature of the force, think of a ray of light as a stream of photons: particles which possess momentum which is proportional to their energy. The proportionality constant is the reciprocal of the speed of light

$$\frac{\text{momentum}}{\text{energy}} = \frac{1}{c} = 3.34 \frac{\text{nN}}{\text{W}} \quad (14)$$

in air. Actually, the units correspond to the *rate of* momentum transfer divided by the *rate of* energy transfer. If all the momentum of the photons were absorbed by the particle, the force felt by the particle is proportional to the power of the beam and the proportionality constant is given by (14).

The force turns out to be quite weak. If you multiply (14) by the energy density typical for normal daytime sunlight reaching the surface of the earth you obtain a radiation pressure of only 10^{-8} atm which is practically imperceptible. Clearly we need to apply a much higher energy density in order to exert measureable forces. With the advent of more powerful lasers in the 1960's, enough photons could be focused on transparent nonabsorbing particles to cause motion [25].

In our experiments, we focus an Ar+ laser beam to a spot size close to the size of the microscopic sphere to obtain energy densities approaching 10^6 W/cm². Photons are not absorbed by our transparent spheres, but scattered. Any change in momentum of the photons owing to their encounter with an object (e.g. reflection, scattering) exerts a force on the object whose magnitude and direction is determined by conservation of momentum.

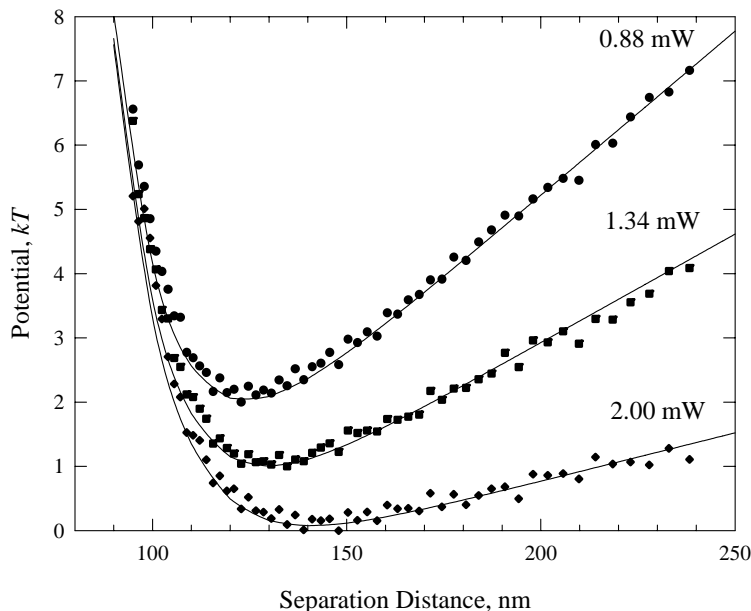


Fig. 13

Total PE profiles measured for a 10 μm PS sphere interacting with a glass slide across a 0.5 mM NaCl solution (replotted from [9]). The three sets of data correspond to different power levels for a laser beam focussed on the bottom of the sphere, producing an upward optical force.

Fig. 13 shows several profiles measured with TIRM for a 10 μm polystyrene latex bead in a 0.5 mM NaCl solution, electrostatically levitated above an ordinary microscope slide. A beam from an argon-ion laser is aimed at the bottom of the sphere and focused to the spot size of about 11 μm diameter. Different power levels for the laser produce the different profiles shown. At large separation distances, the sphere does not interact with the plate and experiences only gravity and optical forces. Over the range of separation distances sampled, both gravity and optical forces are constant, leading to a linear profile whose slope is the apparent weight of the particle. As the power of the beam is increased, the apparent weight decreases owing to an increase in the optical force which is directly upward.

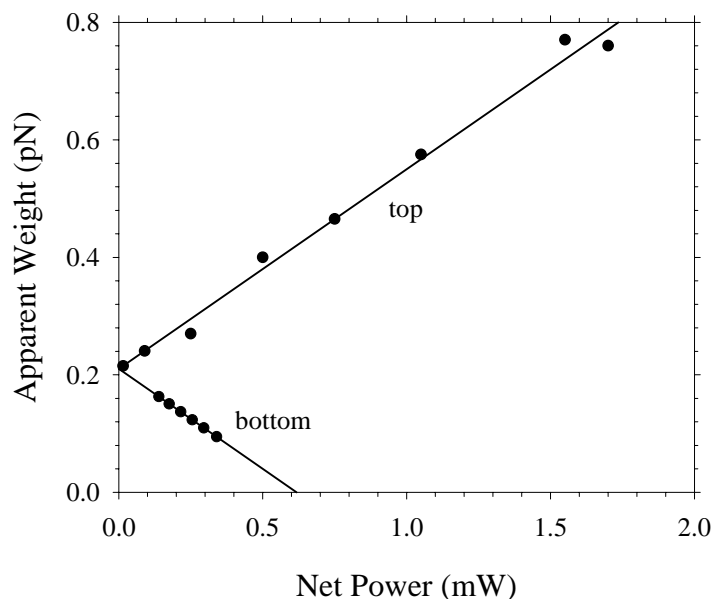


Fig. 14. Effect of the intensity of a 10 μm diameter laser beam, incident on either the top or bottom of a 9 μm PS latex bead in 0.5 mM NaCl solution, on the apparent weight of the particle [26].

Fig. 14 summarizes the results of a systematic study of how the apparent weight depends on the laser power when the beam is incident either on the top or bottom of the sphere. The intercept of either line is the actual net weight of the sphere, 0.21 pN, which agrees well with that calculated from the known size and density. Although the signs are opposite owing to the opposing directions of the two beams, the slope of either regression line is 0.34 nN/W. This value agrees with theoretical predictions (using ray optics) of the optical force exerted by Gaussian beams [27]. Thus optical forces can be accurately predicted using ray optics.

3.4 Other Forces

Liebert & Prieve [28] used TIRM to observe an unexpected long-range attraction between a receptor-ligand pair of proteins. Immunoglobulin G (IgG) was covalently attached to a carboxylated PS latex sphere while protein A (SpA) was covalently attached to a silanated glass slide. IgG and SpA bind to each other in solution with a dissociation constant which depends on the species (goat, horse or rabbit) from which the IgG is obtained. The interactions measured between IgG coated spheres and SpA coated slides displayed a weaker repulsion compared to that observed between bare surfaces under the same conditions. Analysis of the results obtained between the coated surfaces suggest an additional attractive force. This additional attraction does not arise if the IgG-coated sphere is first exposed to a SpA solution so that all the IgG sites are blocked with SpA. The decay length of this attraction correlates with the known dissociation constants for the binding of IgG with SpA in free solution. In summary, the tendency for receptor-ligand pairs to bind causes a long-range (large compared to the dimensions of the proteins) attraction whose decay length increases with the tendency to bind.

Robertson *et al.* [Robertson, 1998 #157] used TIRM to measure the interaction between a glass plate and red blood cells or liposomes. At low ionic strengths, they report profiles like those predicted by (11) and they deduce reasonable values for the weight of the particle and the Debye length. Unfortunately, they cannot obtain absolute separation distances by measuring the intensity of stuck particles since cells and liposomes are highly deformable. One solution is to absorb biologically relevant macromolecules on the surface of nondeformable PS spheres. Robertson & Bike [Robertson, 1998 #156] thus measured the interaction between glass slides and PS spheres coated with mixtures of phospholipids. Once again they report profiles like those predicted by (11); but having the absolute separation distance, they can now deduce the surface potential of the sphere as a function of the composition of the phospholipid mixture or pH.

Sober & Walz [29] used TIRM to measure the depletion attraction caused by the exclusion of CTAB micelles from the gap between the sphere and the plate. Owing to the exclusion from the gap, the osmotic pressure of the solution there is lower than over the remainder of the surface of the sphere. Integrating the osmotic pressure over the sphere surface yields a net force on the sphere acting to push it toward the glass slide. Compared to earlier measurements with SFA [30] or AFM [31], much weaker depletion interactions can be studied with TIRM. This means that much lower concentrations of the depletent can be used. For example, Pagac *et al.* [32] have detected significant depletion attraction in solutions containing only 5 ppm of polylysine (179 kDa) while Odiach and Prieve[33] have detected significant depletion attraction in solutions containing as little as 100 ppm of a synthetic clay.

The osmotic pressure of polyelectrolytes tends to be orders of magnitude larger than the same molar concentration of uncharged macromolecules [33]. In contrast to the above studies, which involve polyelectrolytes, Rudhardt *et al.*[34] observed significant depletion attraction with TIRM using 30 ppm of poly(ethylene oxide) with a molecular weight of 2×10^6 under conditions in which the radius of gyration is expected to be 100 nm.

Haughey and Earnshaw[14] applied a voltage between glass plates coated indium-doped tin oxide (ITO) to generate an electric current of the order of a few $\mu\text{A}/\text{cm}^2$ through the solution normal to the plate. This electric current had a significant effect on the apparent weight of the particle and its most probable elevation measured with TIRM. Making the plate at which the evanescent wave is generated more negative (particle is also negatively charged) made the particle appear lighter and increased the most probable elevation, while making the plate more positive had the opposite effect. Haughey and Earnshaw also report TIRM measurements of oil drops.

4. Results: Dynamics

Until now, we have focussed on measuring colloidal interactions with TIRM. PE profiles are obtained from the equilibrium distribution of elevations sampled by the sphere (recall Fig. 9). The time at which instantaneous elevations were sampled is discarded in this analysis. However, the rate of change in elevation contains additional information concerning the dynamics of Brownian motion of the sphere. We will now review experiments which focus on dynamics.

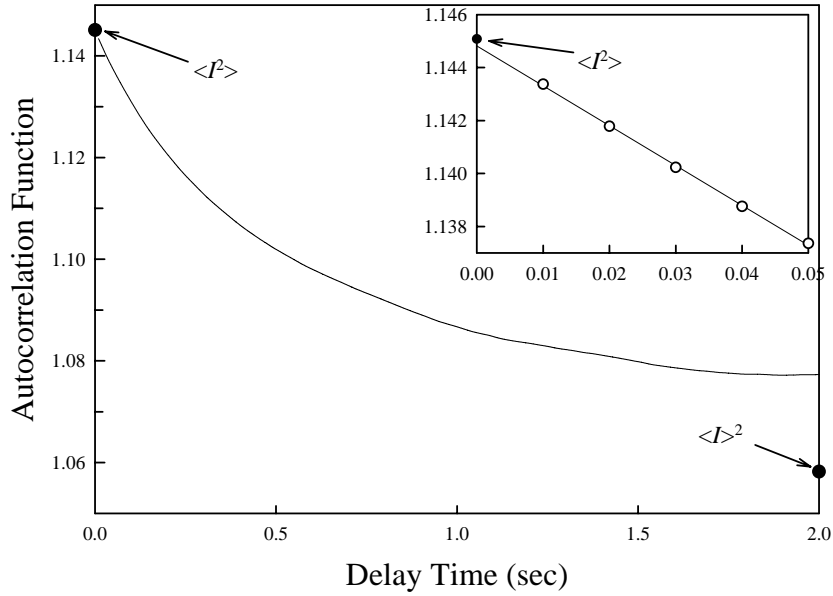


Fig. 15

The intensity autocorrelation function of a 10 μm PS sphere in 0.1 mM KCl. The insert shows the linearity of the short-time data used to compute the diffusion coefficient.

4.1 Hindered Diffusion

One method to analyze the dynamics of random fluctuations (like those of Fig. 8) is to compute the associated intensity autocorrelation function, which is defined as

$$R(\tau) = \langle I(t)I(t+\tau) \rangle \equiv \lim_{T \rightarrow \infty} \left[\frac{1}{T} \int_{t_0}^{t_0+T} I(t)I(t+\tau) dt \right] \quad (15)$$

where $I(t)$ is the fluctuating intensity. From the second equality, we see that the carets $\langle \dots \rangle$ denote the average with respect to different starting times t . As long as we are sampling a stationary distribution long enough, this average should not depend on the initial starting time t_0 . Then the time-average of the product of the intensities is a function only of the delay time τ .

Fig. 15 shows a typical autocorrelation function computed from data like those in Fig. 8. When $\tau = 0$, (15) yields $R(0) = \langle I^2 \rangle$. On the other hand, when $\tau = \infty$, $I(t+\tau)$ is totally independent of $I(t)$; then (15) yields $R(\infty) = \langle I \rangle^2$ [35]. The values of $\langle I^2 \rangle$ and $\langle I \rangle^2$ are also shown for comparison in Fig. 15. Typically the autocorrelation function undergoes a monotonic decay from $\langle I^2 \rangle$ to $\langle I \rangle^2$. Fig. 15 might be called a memory function, because the time it takes

$R(\tau)$ to decay to its asymptotic value is the time it takes the sphere to forget its original location at time t . The particle in Fig. 15 forgets its previous position in about one or two seconds.

If each observation of $I(t)$ is to be independent of the previous measurement, we should sample at about one-second intervals. Then the uncertainty in the number of counts N in any bin of the histogram of Fig. 9 could be estimated as \sqrt{N} . The corresponding uncertainty in the PE associated with this bin is kT/\sqrt{N} . By sampling at a higher frequency, we have accepted some redundancy in our data collection and the uncertainty in PE values is larger than kT/\sqrt{N} .

In the usual dynamic light scattering experiment, each of the hundred or so particles in the sample volume is illuminated uniformly. Fluctuations in scattering intensity arise because changes in the relative positions of individual particles by Brownian motion causes changes in the interference of light rays scattered by those particles. For dilute suspensions of noninteracting particles, the autocorrelation function is a simple exponential decay whose initial slope is inversely proportional to the diffusion coefficient of the particles. Although the situation in TIRM is quite different (we have one particle experiencing nonuniform illumination rather than many particles uniformly illuminated), the initial slope of the autocorrelation function is also inversely proportional to the diffusion coefficient [35]:

$$\lim_{\tau \rightarrow 0} \left\{ \frac{R(\tau)}{R(0)} \right\} = 1 - \beta^2 D_{app} \tau$$

where β^{-1} is the penetration depth for the evanescent wave [see (3)]. Since the diffusion coefficient depends on position in the TIRM experiment, D_{app} is a weighted-average of the diffusion coefficients experienced by the particle in sampling different elevations by Brownian motion:

$$D_{app} = \frac{\int_0^{\infty} D(h) e^{-2\beta h} p(h) dh}{\int_0^{\infty} e^{-2\beta h} p(h) dh}$$

Note that the weighting function is not just the Boltzmann factor $p(h)$ but it is the Boltzmann factor multiplied by the square of the local intensity $I^2(h) p(h)$.

For the data in Fig. 15, D_{app} turns out to be only 3.9% of the Stokes-Einstein value for a 10 μm sphere in water. The sphere is very close to the wall, so that its motion is severely hindered by hydrodynamic drag on the wall. The amount of the decrease in mobility was predicted by Brenner and Cox [36, 37].

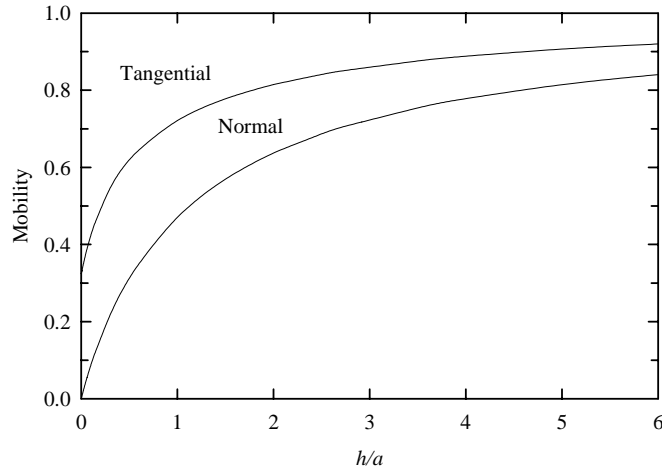


Fig. 16

Hydrodynamic hinderence of a sphere of radius a located at elevation h above a rigid wall. Upper curve is for motion of the sphere tangential to the wall [37] while lower curve is for motion normal to the wall [36]. The mobility has been normalized by its value far away from the wall ($h/a \rightarrow \infty$).

Fig. 16 shows the sphere's mobility normalized by its value infinitely far from the wall, as a function of the distance from the wall divided by the sphere's radius. The amount of the decrease is different for motion normal to the wall versus motion tangential to the wall, but both mobilities tend to vanish as the sphere comes into contact with the wall. With TIRM, we are observing motion normal to the wall. The separation distance in our experiments corresponds to h being a few percent of its radius a , so we are expecting our mobility to be severely hindered.

According to Einstein's equation, the diffusion coefficient should also be hindered by the same fraction as the mobility:

$$D(h) = m(h) kT \quad (16)$$

So let's test this hypothesis. If it's correct, anything which changes the separation distance ought to change the diffusion coefficient. One experimental variable we can change is the salt concentration, which ought to affect the most probable separation distance by weakening double-layer repulsion.

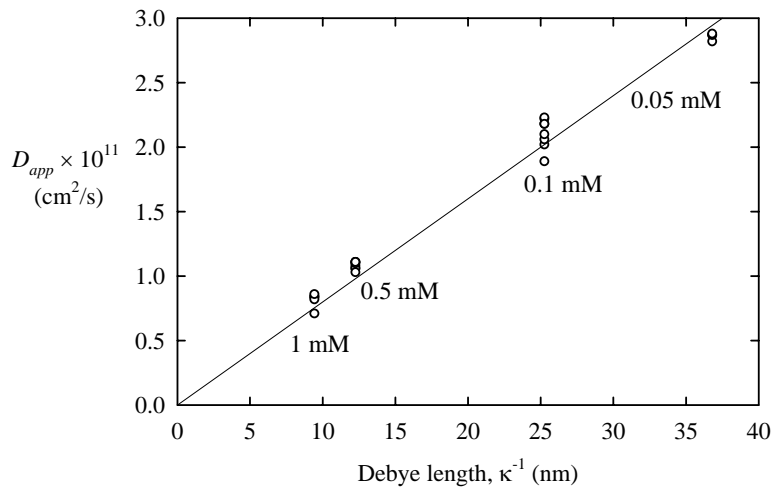


Fig. 17

Effect of salt concentration (expressed in terms of the Debye length) on the average diffusion coefficient of a 10 μm PS latex particle deduced from the autocorrelation function (adapted from Fig. 10 of [35]). The solid curve is the predicted diffusion coefficient if the sphere were located at 8.2 Debye lengths above the plate.

Fig. 17 shows the values of the diffusion coefficients that we measured for a number of different 10 μm spheres in solutions having different salt concentrations. The salt concentration is written next to each cluster of points. Notice that the diffusion coefficient decreases as the salt concentration goes up. This is because the addition of salt compresses the double layer, so the particle must come closer to the plate to experience a repulsion which equal to its weight. The solid line is what we would expect to see if the sphere was levitated at 8.2 Debye lengths above the plate for all salt concentrations. This separation distance is in line with optical measurements of the separation distance; for example, the minimum in Fig. 10 occurs at 9.3 Debye lengths. The variations among different particles in any cluster are probably due to differences in the charge on the particles which, according to (10), is expected to affect the most probable separation distance less sensitively than the Debye length itself.

Knowing how the proximity to the wall affects the sphere's mobility and diffusion coefficient (see Fig. 16), we can use the measured D_{app} to infer an average elevation of the particle above the plate, which we denote as h_{app} . This hydrodynamic average elevation is somewhat different from the most probable elevation h_m by an amount which can be calculated if the PE profile has the form of (6) [35]. After correcting for the difference, Fig. 18 compares the hydrodynamic measure of the elevation with that obtained independently from the brightness of the sphere for three different sizes of spheres. Note that the two measures of elevation agree very closely.

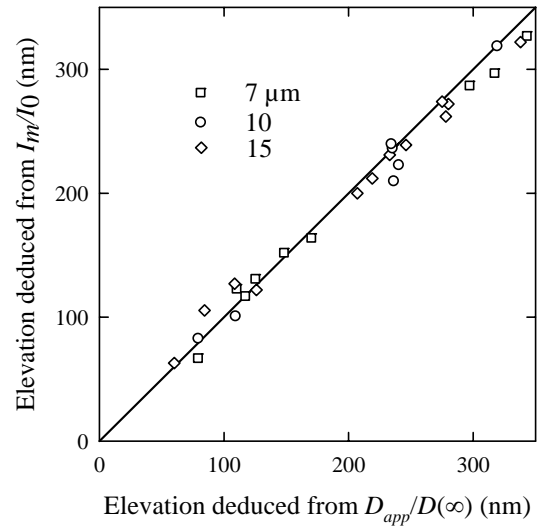


Fig. 18
A comparison of the elevation h_m , deduced from the brightness of the levitated sphere with the elevation deduced from the average diffusion coefficient (adapted from Fig. 12 of [35]).

This agreement is significant in that it tends to confirm Einstein's equation (16) relating mobility and diffusion coefficient since (16) was used in conjunction with Brenner's prediction of how the mobility of the sphere is related to elevation. To our knowledge, these are the first observations of Brownian motion of a single sphere, in a colloidal force field, very near to a wall, where such hinderence effects are severe.

4.2 Hindered Mobility

In addition to the diffusion coefficient, TIRM is also capable of independently measuring the hydrodynamic mobility m of the Brownian sphere. By observing the initial rate of change of elevation in response to a step-change in the axial component of the optical force, the mobility of the sphere can be deduced. This was first performed with TIRM by Brown and Staples [38, 39] who used the measured mobility to infer the absolute separation distance.

A systematic study of mobility versus separation distance was undertaken by Pagac *et al.* [40]. The results of mobility measurements at different ionic strengths and for two different sizes of particles, are summarized by Fig. 19. All of the measured mobilities lie within experimental error of the solid curve, which represents the theory of Brenner [36].

5. Comparison with Other Techniques

Now that we have seen how TIRM works, let's compare it's capabilities with two more familiar techniques for measuring forces. Probably the best-known technique is the Surface-Forces Apparatus developed by Jacob Israelachvili [41]. This apparatus allows direct measurement of the surface forces between two macroscopic crossed cylinders which are made atomically smooth: see Fig. 20. The distance between the surfaces can be measured to an angstrom using interferometry. The force is measured by deflection of a spring.

Note that the surface forces apparatus measures the interaction of macroscopic bodies on the order of 1 cm in size, whereas colloidal particles of interest are several orders of magnitude smaller in size. Of course, you can use Derjaguin's approximation to scale the measurements made here to other geometries like two microscopic spheres or a sphere and a plate.

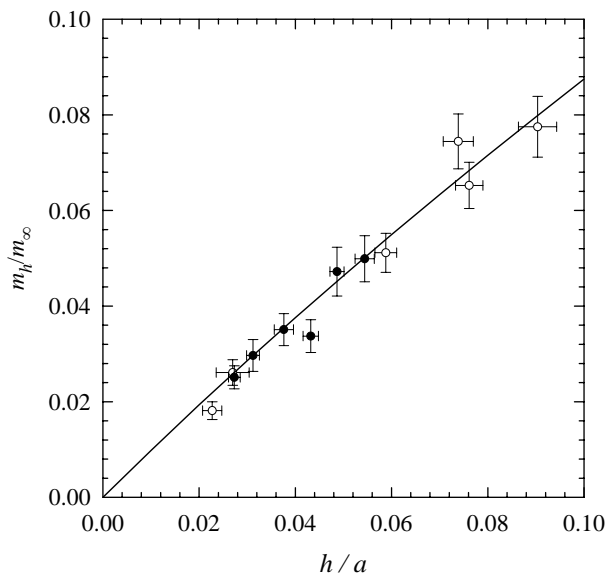


Fig. 19
Mobilities measured for 7 μm (open circles) and 10 μm (filled circles) PS particles in either distilled water or solutions containing 0.1 mM or 1 mM NaCl.

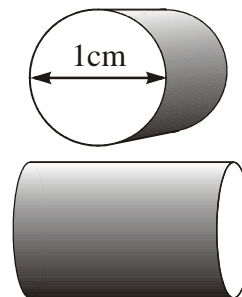


Fig. 20
SFA measures the interaction between crossed cylinders having a curvature on the order of 1 cm.

In 1992 Ducker *et al.* [42] attached a single 7-micron silica particle to the tip of an Atomic Force Microscope and then measured its interaction with a flat silicon wafer from the deflection of the AFM cantilever: see Fig. 21. Many other labs are now using this technique, which has the advantage that one of the interacting bodies is at least microscopic if not colloidal in size.

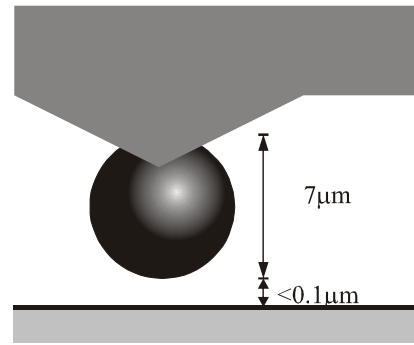


Fig. 21
AFM measures the interaction between a microscopic sphere and a flat plate.

In both AFM and SFA, the two bodies are mechanically held a fixed but controllable distance apart while the force is being measured. This arrangement is well suited for measuring the equilibrium interaction of the two bodies. But real colloidal particles of commercial interest undergo Brownian motion and the distance between them continually fluctuates. Then the equilibrium interaction might not be the relevant one. This is particularly true of colloidal dispersions which are stabilized by steric repulsion of physisorbed polymer layers, whose conformation can be disturbed by the squeezing flow which occurs when two interacting bodies move toward or away from one another by Brownian motion.

Using TIRM we are measuring the dynamic interactions which occur during Brownian motion. In this sense, TIRM is measuring interactions which are more characteristic of colloidal dispersions. In fact, this is probably the most important advantage TIRM over the other techniques.

Now let's turn to a more quantitative comparison of the techniques. The numbers in Table 1 represent resolutions in force or distance which have been reported in the literature by authors who first used each respective technique. Note that SFA has the best spatial resolution of any technique. The resolution in separation distance of both AFM and TIRM will be ultimately limited by the roughness on the surface of the microscopic sphere; by contrast, SFA uses atomically smooth mica sheet for both surfaces.

Quantity	SFA	AFM	TIRM
Separation Distance (nm)	0.1	1	1
Force (N)	10^{-9}	10^{-11}	10^{-14}
Energy per Area (J/m^2)	10^{-7}	10^{-6}	10^{-9}

Table 1
A comparison of the resolution of the three techniques for measuring colloidal interactions.

On the other hand, both AFM and TIRM have a better resolution in the force than SFA. Of course, that greater sensitivity is really needed, since the forces on a microscopic sphere are orders of magnitude weaker than between two macroscopic bodies. A fairer basis of comparison might be the force divided by the characteristic radius of the interacting bodies: using

Derjaguin's approximation, the force divided by the radius equals the energy per unit area between two infinite parallel plates. On this basis, AFM is not as good as SFA, but TIRM is actually two orders of magnitude more sensitive than either SFA or AFM. The reason TIRM is so much more sensitive is that it uses a molecular gauge for energy (kT) rather than a mechanical gauge for force (spring constant).

While TIRM is capable of measuring much weaker interactions, it is incapable of measuring interactions as strong as some reported for AFM or SFA: when the attraction between the sphere and the plate become very strong, the apparent PE profile deduced from TIRM (compare with Fig. 10) becomes a narrow parabola whose width is ultimately limited by noise in the light detection system, rather than the actual PE profile. Thus strong attractions are masked in TIRM by noise. Of course, the “weak” interactions which can be measured by TIRM are also the ones responsible for colloid stability. Recalling Fuchs' equation for the stability ratio

$$W = 2a \int_{2a}^{\infty} \exp\left[\frac{\phi(r)}{kT}\right] \frac{dr}{r^2}$$

we estimate that energy barriers as “weak” as $10kT$ can produce a stable dispersion [43]. Thus it is only the first few kT of the interaction which is relevant to colloid stability; this is exactly the order of magnitude of interactions which can be measured by TIRM.

5.1 Related Techniques for Measuring Microsphere-Plate Interactions

Another technique closely related to TIRM is Evanescent Wave Light Scattering (EWLS) [44]. The scattering from a suspension of particles, illuminated by an evanescent wave, is measured as a function of penetration depth. If enough penetration depths are used, the results might be directly inverted to obtain particle concentration versus elevation. This technique has the important advantage that sub-micron particles can be used provided the concentration is high enough for significant scattering. In the implementation of Ref. [44], an impinging-jet flow was imposed over the surface. This complicates the interpretation by applying hydrodynamic forces on the particles. Instead of directly inverting the intensity-versus-penetration-depth data, the concentration profiles presented in [44] are those predicted by solving the one-dimensional convective-diffusion-migration equation for various assumed PE profiles which lead to predictions of scattering which most closely fit that observed; thus, as implemented, EWLS is an indirect method of determining PE profiles. Moreover, using Boltzmann's equation to interpret the concentration profile in terms of the PE profile requires the assumption that all the particles are equivalent (and do not interact with one another) and the plate has spatially uniform properties.

Kepler and Fraden [45] measured the 3D distribution of $1.27 \mu\text{m}$ PS spheres confined between two parallel glass plates whose separation was varied between $4 \mu\text{m}$ and $8.4 \mu\text{m}$. The elevation (z) relative to the focal plane of the microscope objective lens was determined to ± 70 nm from the intensity of the particles. The lateral position within the xy plane was determined by video microscopy. At the very low ionic strengths, maintained by continuous ion exchange, particles distributed along the z -axis in a Gaussian manner, with the standard deviation

increasing with the separation distance between the two parallel glass plates. Reasonable values for the Debye length and surface potentials were deduced from these experiments.

5.2 Techniques for Measuring Microsphere-Microsphere Interactions

Several other techniques have been proposed which allow measurement of the interaction when the plate is replaced by a second microscopic particle. Bibette *et al.*[46] measured the interaction between 190-nm octane ferrofluid droplets in water by applying a magnetic field to align the droplets in a long chain. The separation distance is measured as a function of magnetic field strength using Bragg diffraction. Knowing the magnetic properties of the droplets allows them to compute the magnetic attraction as a function of magnetic field strength. Assuming the separation distance corresponds to equivalence of attractive and (electrostatic) repulsive forces allows the repulsive force to be measured as a function of separation distance. Although elegant, the obvious disadvantage of this technique is that it can only measure the interaction between ferrofluid droplets.

Crocker and Grier [47] use two micromanipulated optical tweezers to bring two like-charged 0.75 μm PS particles close together. Turning off the tweezers, the separation distance is determined as a function of time using video microscopy to follow their drifting apart. Analysis of the video images allows them to determine the separation distance to about 25 nm. Repeating the experiment about 800 times allows them to deduce the PE profile. A similar “blinking optical tweezers” technique has also been used by Ou-Yang *et al.* [48]. Using video microscopy, the separation between particle centers can be determined with an uncertainty that is well below the diffraction limit for visible light; however, the uncertainty in separation distance is still an order of magnitude greater than that for SFA, AFM or TIRM.

In “colloidal particle scattering” [49], the cumulative interaction between two nearly identical 3-5 μm PS particles, one stuck to a glass plate and the other entrained in linear shear flow tangent to the plate, is determined from the displacement of the trajectory of the moving particle caused by encountering the stuck particle. Hydrodynamic interactions at very low Reynolds numbers are completely reversible: hydrodynamic repulsion experienced during approach of two particles becomes hydrodynamic attraction during their eventual separation. As an entrained particle encounters a stuck particle, its trajectory deviates from a straight line to avoid collision with the stuck particle. Once past the stuck particle, an entrained particle experiencing purely hydrodynamic interactions with the stuck particle resumes its linear trajectory with no net displacement from the original straight line. On the other hand, colloidal forces are not reversible: colloidal repulsion experienced during approach remains repulsive during separation, leading to a net displacement of the trajectory. End views of the initial and final linear trajectories are each plotted as single points on a polar graph relative to the center of the stuck particle. This is repeated for 10's of encounters of different entrained particles with the stuck particle. Displacements away from the center of the stuck particle indicate repulsion while displacements toward the center indicate attraction. The net displacement resulting from each encounter depends on a convolution of the position-dependent forces and the position-dependent mobility over the range of separation distances experienced during that encounter. While deconvolution to obtain the force-versus-distance profile from many encounters might be possible, the results to date have been analyzed by comparisons with theoretical predictions

assuming a functional form for the interactions. In this mode, colloidal particle scattering is an indirect technique.

6. Measurements on Smaller Particles

Ten microns is near or above the upper size most researchers would include when defining a colloids. So a frequent question is “can TIRM be used with smaller particles?” Smaller particles generally scatter less light. Fig. 22 summarizes the measurement of average scattering intensity of stuck particles as a function of particle size. Although there is some scatter in the data points (which were obtained on different days), the slope on this log-log plot indicates the dependence on diameter is less than first power.

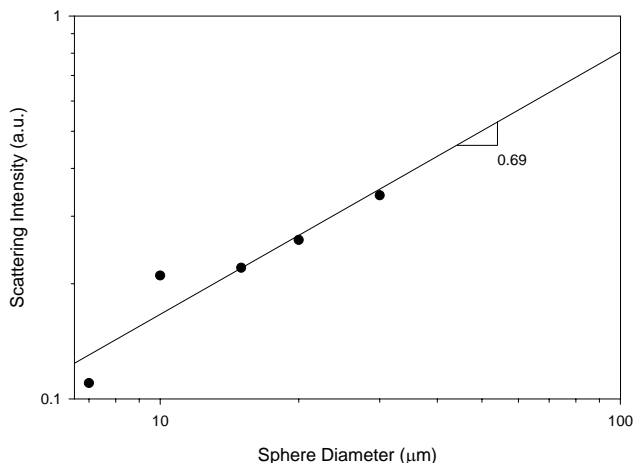


Fig. 22

Effect of particle size on the scattering of PS spheres “stuck” to a MgF_2 film in alcohol and illuminated by an evanescent wave [7]. The solid line is a linear regression.

However, smaller particles also tend to reside further above the plate. The 10- μm particle in Fig. 10 experienced a most-probable elevation distance of 120 nm. According to (10), if we reduced the size to 1 μm , keeping all other properties fixed, the most probable elevation increases to 182 nm. More important still is the range of separations sampled by Brownian motion. Owing to a much shallower slope in the gravity-dominated portion of the profile, a 1 μm PS particle would have to reach almost 90 μm above the plate before its PE increases to $6 kT$. Throughout most of this range, the small particle would not scatter enough of the evanescent wave to be visible on the background.

A simple solution is to drastically reduce the range of the Brownian excursions by pushing down on the particle using optical force described in Section 3.3. Applying optical forces comparable to the buoyant weight of a 10 μm PS bead should result in excursions with a range similar to that sampled by a free 10 μm PS bead. Of course, a 1 μm PS bead is still expected to scatter less light, but an order of magnitude reduction should still be measurable.

Rudhardt *et al.*[50] report measurements of the interaction with a 3 μm PS latex particle and a fused silica plate at very low ionic strengths (3.5-110 μM) and a much longer penetration depth. Although the net weight of the particle agrees with that expected, the best-fitting Debye length is 40% larger than predicted for the lowest ionic strength. Since ionic strength is taken to be the measured specific conductance divided by the equivalent conductance for NaCl, any dissolved CO_2 will make the solution acidic and thereby increase the average equivalent conductance: typical distilled deionized water has a pH around 6, which corresponds to an ionic strength of 1 μM . Tanimoto *et al.*[51] report measurements of the interaction with a one-micron

PS latex particle. Unfortunately, no quantitative analysis of the PE profiles was performed and the qualitative trends with ionic strength are not consistent with those expected from (6).

References

- [1] D. C. Prieve, F. Luo and F. Lanni, *Faraday Disc.*, 83, (1987) 297.
- [2] D. C. Prieve and B. M. Alexander, *Science*, 231, (1986) 1269.
- [3] B. M. Alexander and D. C. Prieve, *Langmuir*, 3, (1987) 788.
- [4] S. G. Lipson and H. Lipson, *Optical Physics*. Cambridge University Press, New York, 1982.
- [5] H. Chew, D. S. Wang and M. Kerker, *Applied Optics*, 18, (1979) 2679.
- [6] I. N. Court and K. V. Willisen, *Applied Optics*, 3, (1964) 719.
- [7] D. C. Prieve and J. Y. Walz, *Applied Optics*, 32, (1993) 1629.
- [8] R. L. B. Liebert, PhD Dissertation, Carnegie Mellon University (1995).
- [9] J. Y. Walz and D. C. Prieve, *Langmuir*, 8, (1992) 3043.
- [10] J. Y. Walz, PhD Dissertation, Carnegie Mellon University (1992).
- [11] T. Nagase, PhD Dissertation, Carnegie Mellon University (1995).
- [12] D. C. Prieve and N. A. Frej, *Langmuir*, 6, (1990) 396.
- [13] L. A. Spielman, *J. Colloid Interface Sci.*, 33, (1970) 562.
- [14] D. Haughey and J. C. Earnshaw, *Colloids and Surfaces A*, 136, (1998) 217.
- [15] I. Larson, C. J. Drummond and D. Y. C. Chan, *J. Amer. Chem. Soc.*, 115, (1993) 11855.
- [16] I. Larson, PhD Dissertation, University of Melbourne (1996).
- [17] P. G. Hartley, I. Larson and P. J. Scales, *Langmuir*, 13, (1997) 2207.
- [18] S. G. Bike and D. C. Prieve, *Int. J. Multiphase Flow*, 16, (1990) 727.
- [19] S. G. Flicker and S. G. Bike, *Langmuir*, 9, (1993) 257.
- [20] S. G. Flicker, J. L. Tipa and S. G. Bike, *J. Colloid Interface Sci.*, 158, (1993) 317.
- [21] M. A. Bevan and D. C. Prieve, *Langmuir*, , (submitted) .

- [22] V. A. Parsegian, in *Physical Chemistry: Enriching Topics from Colloid and Surface Science* K. J. Mysels, Ed. (Theorex, La Jolla, CA, 1975) pp. 27.
- [23] B. A. Pailthorpe and W. B. Russel, *J. Colloid Interface Sci.*, 89, (1982) 563.
- [24] L. Suresh and J. Y. Walz, *J. Colloid Interface Science*, 196, (1997) 177.
- [25] A. Ashkin, *Phys. Rev. Lett.*, 24, (1970) 156.
- [26] R. L. B. Liebert, D. Desrosiers and D. C. Prieve, in preparation, .
- [27] R. B. Liebert and D. C. Prieve, *Ind. Eng. Chem. Res.*, 34, (1995) 3542.
- [28] R. B. Liebert and D. C. Prieve, *Biophys. J.*, 69, (1995) 66.
- [29] D. L. Sober and J. Y. Walz, *Langmuir*, 11, (1995) 2352.
- [30] P. Richetti and P. Kekicheff, *Phys. Rev. Lett.*, 68, (1992) 1951.
- [31] A. Milling and S. Biggs, *J. Colloid Interface Sci.*, 170, (1995) 604.
- [32] E. S. Pagac, D. C. Prieve and R. D. Tilton, *Langmuir*, 13, (1997) 2993.
- [33] P. C. Odiachi and D. C. Prieve, *Colloids and Surfaces A*, , (accepted) .
- [34] D. Rudhardt, C. Bechinger and P. Leiderer, *Phys. Rev. Lett.*, 81, (1998) 1330.
- [35] N. A. Frej and D. C. Prieve, *J. Chem. Phys.*, 98, (1993) 7552.
- [36] H. Brenner, *Chem. Eng. Sci.*, 16, (1961) 242.
- [37] A. J. Goldman, R. G. Cox and H. Brenner, *Chem. Engr. Sci.*, 22, (1967) 637.
- [38] M. A. Brown, A. L. Smith and E. J. Staples, *Langmuir*, 5, (1989) 1319.
- [39] M. A. Brown and E. J. Staples, *Langmuir*, 6, (1990) 1260.
- [40] E. S. Pagac, R. D. Tilton and D. C. Prieve, *Chemical engineering communications.*, 148, (1996) 105.
- [41] J. N. Israelachvili and G. E. Adams, *J.C.S. Faraday I*, 74, (1978) 975.
- [42] W. A. Ducker, T. J. Senden and R. M. Pashley, *Langmuir*, 8, (1992) 1831.
- [43] D. C. Prieve and E. Ruckenstein, *J. Colloid Interface Sci.*, 73, (1980) 539.
- [44] M. Polverari and T. G. M. van de Ven, *Langmuir*, 11, (1995) 1870.
- [45] G. M. Kepler and S. Fraden, *Langmuir*, 10, (1994) 2501.

- [46] F. L. Calderon, T. Stora, O. M. Monval, P. Poulin and J. Bibette, *Phys. Rev. Lett.*, 72, (1994) 2959.
- [47] J. C. Crocker and D. G. Grier, *Phys. Rev. Lett.*, 73, (1994) 352.
- [48] M. T. Valentine, L. E. Dewalt and H. D. Ou-Yang, *J. Physics: Condensed Matter (UK)*, 8, (1996) 9477.
- [49] T. G. M. van de Ven, P. Warszynski, X. Wu and T. Dabros, *Langmuir*, 10, (1994) 3046.
- [50] D. Rudhardt, C. Bechinger and P. Leiderer, *Progr. Colloid Polym. Sci.*, 110, (1998) 37.
- [51] S. Tanimoto, H. Matsuoka and H. Yamaoka, *Colloid Polymer Sci.*, 273, (1995) 1201.

Table of Contents

1. INTRODUCTION	2
2. THE TECHNIQUE	2
2.1 MEASURING THE POTENTIAL	3
2.2 MEASURING THE SEPARATION DISTANCE	4
2.3 APPARATUS	7
2.4 ANALYSIS OF DATA	10
3. RESULTS: PE PROFILES.....	12
3.1 GRAVITY AND DOUBLE-LAYER REPULSION.....	12
3.2 VAN DER WAALS ATTRACTION	16
3.3 OPTICAL FORCES	17
3.4 OTHER FORCES	19
4. RESULTS: DYNAMICS.....	20
4.1 HINDERED DIFFUSION.....	21
4.2 HINDERED MOBILITY.....	25
5. COMPARISON WITH OTHER TECHNIQUES	26
5.1 RELATED TECHNIQUES FOR MEASURING MICROSPHERE-PLATE INTERACTIONS.....	28
5.2 TECHNIQUES FOR MEASURING MICROSPHERE-MICROSPHERE INTERACTIONS.....	29
6. MEASUREMENTS ON SMALLER PARTICLES	30
REFERENCES	31
TABLE OF CONTENTS	1